

A 16 × 24 Germanium photoconductor array for AIRES

Jessie Dotson^a, Edwin Erickson^b, Michael R. Haas^b, David Rabanus^c, and James A. Baltz^d

^aSETI Institute, MS 245-6, Moffett Field, CA, USA

^bNASA Ames Research Center, MS 245-6, Moffett Field, CA, USA

^cDLR, MS 245-6, Moffett Field, CA, USA

^dSverdrup, MS 245-6, Moffett Field, CA, USA

ABSTRACT

We have designed and prototyped an array of Ge:Sb photoconductors for use in AIRES, the Airborne InfraRed Echelle Spectrometer, on SOFIA. The 16×24 flight array will operate between 33 μm and 120 μm . In this paper we discuss the testing of a 3×3 prototype array and the resulting design of the flight array.

Keywords: Far-Infrared Detectors, Astronomical Airborne Instrumentation

1. INTRODUCTION

AIRES, the Airborne InfraRed Echelle Spectrometer, will be operated as a first generation, general purpose facility instrument on SOFIA. At first light, its operating wavelength range for spectroscopy is planned to be 30 to 120 μm . There will be a 2 to 28 μm slit viewer. AIRES is a long slit spectrometer with a rotating K-mirror, allowing simultaneous observations of the spectrum along a user-selectable strip of the sky. The spectral resolution will vary between $4.0 \times 10^5/\lambda$ to $1.1 \times 10^6/\lambda$ where λ is the wavelength in μm . AIRES will be ideal for spectral imaging of gas-phase phenomena in the interstellar medium (ISM). Far-infrared line observations probe the excitation, pressure, density, luminosity, chemical composition, heating and cooling rates, mass distribution, and kinematics in the various components of the ISM. These lines offer invaluable and often unique diagnostics of conditions in such diverse objects as star forming regions, circumstellar shells, the Galactic Center, starbursts in galaxies, and the nuclei of active galaxies. AIRES will provide new insights into these and other environments in the ISM.

In order to assure we have the best detectors for our application, we have designed, built, and tested a 3×3 prototype array. For comparison we have simultaneously tested a 1×32 array developed for the MIPS instrument in SIRTF¹⁻³ and 6 detectors from the Cooled Grating Spectrometer (CGS).^{4,5} The CGS is an echelle spectrometer which flew for 15 years on the Kuiper Airborne Observatory. Much of AIRES' design is based on the CGS. The three arrays were mounted simultaneously in the focal plane of the CGS during testing. The tested arrays have several significant differences: 1) material, 2) methods for concentrating light on the detectors, 3) light collecting area, and 4) detector volumes/geometries. We consider these differences when interpreting our results.

2. ARRAY DESCRIPTION

The AIRES detectors are discrete 1mm × 1mm × 2.5mm house shaped chips of Ge:Sb. Each detector is mounted in an oblong cavity which is sitting behind a straight sided cone with a 2mm × 2mm collecting area. The AIRES prototype design is discussed in Ref. 6 and is shown in Fig. 1.

The SIRTF array is a 0.5mm × 25.5mm × 2mm monolithic bar of Ge:Ga. The individual pixels are delineated along the bar by the signal wires which are spaced at 0.75mm. The light is focused onto the detectors by a Ge lenslet. The collecting area of each pixel is 0.75mm × 0.75mm.¹

The CGS detectors are discrete 2mm × 2mm × 1.5mm rectangular pieces of Ge:Sb. The individual pixels each sit in a cylindrical cavity. The light is focused to the entrance aperture of the cavity by field mirrors. The collecting area is 10mm × 2mm.

Further author information: (Send correspondence to J.D)
J.D. E-mail: dotson@cygnus.arc.nasa.gov

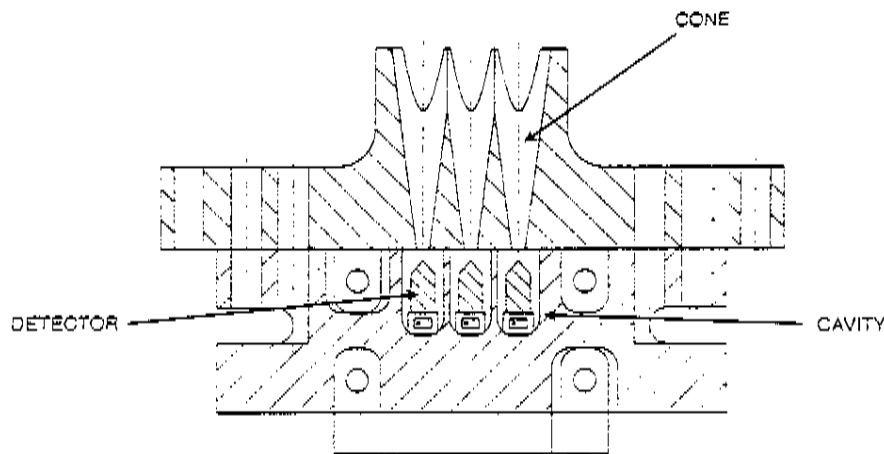


Figure 1. Section of the prototype 3x3 AIRE array. The straight-sided, close-packed cones concentrate the light into the oblong cavities. The house shaped Ge:Sb detectors are mounted within the cavities.

3. RESULTS

Measurements were made with the three detector sets mounted simultaneously in the CGS. Some absolute measurements were made. However, comparing relative detector performance allows us to compare the performance of the arrays without the added uncertainty of accounting for the precise behavior and transmission of the test source and instrument. Here we present a subset of our results. After describing the test apparatus and methods, we discuss how the arrays' performance varies with wavelength. We also discuss the noise regime the arrays are operating in and conclude by presenting our relative noise equivalent power (NEP) measurements.

3.1. Test Apparatus

All measurements were made with the CGS.^{4,5} The detectors were readout with transimpedance amplifiers (TIAs). The unit cell is shown in Fig. 2. Most measurements were made with the CGS data system and preamps. In some situations we directly measured the offset (the DC voltage difference from the bias voltage) at the test point. Unless otherwise specified measurements were made at 88 μm . The signal measurements were made of a large chopped blackbody source which was focused by a mirror installed in a vacuum chamber. Signal measurements were made in a *high* background configuration through a 7mm aperture. Noise measurements were made in both the *high* background and *low* background configuration. In the *low* background configuration a mirror was placed in front of the instrument window so that the instrument would be looking back into itself.

Since each detector set has a different collecting area, a different flux level is seen by each array. The throughput for each array is given by $A\Omega\delta\lambda$, where A is the effective collecting area of the detector, Ω is the solid angle seen by the detector, and $\delta\lambda$ is the size of the wavelength increment seen by the detector. The effective collecting area is a function of the instrument's optics as well as the geometric collecting area of each detector. The measured effective collecting areas are shown in Table 1. The solid angle for the background was confirmed. The grating equation was used to calculate $\delta\lambda$. The resulting values are shown in Table 1.

The instrument throughputs in Table 1 can be used to estimate the signal and high background fluxes. The high background flux is obtained by assuming the background is coming from a room temperature blackbody and using a transmission for the CGS of 0.24.⁴ The signal flux was reduced by warm black polyethylene filters. A filter was sized to provide a reasonable signal to noise ratio for each detector set. The signal flux is estimated from the temperature of the blackbody source (1073K) and the total instrument transmission for each array ($\tau_{\text{CGS,aires}} = 1.7 \times 10^{-4}$).

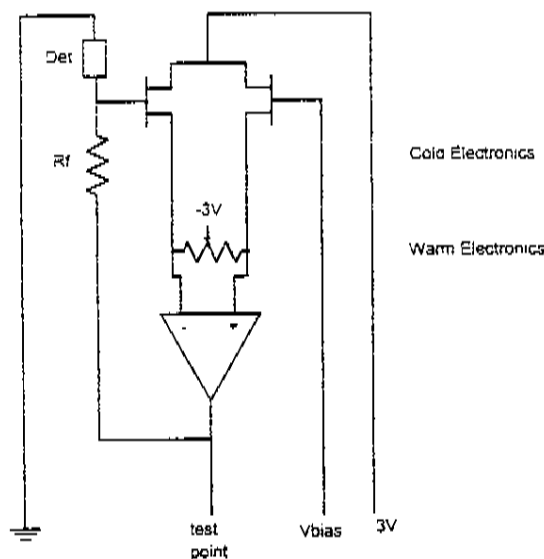


Figure 2. The TIA unit cell. All components above the dotted line are in the dewar and operate near 3K.

Table 1. Instrument Throughput at 88 μm

Array	A (mm^2)	Ω_s (sr)	Ω_b (sr)	$\delta\lambda$ (μm)	Absolute ($\text{mm}^2 \text{sr } \mu\text{m}$)		Relative to SIRTf
					T_s	T_b	T_s, T_b
AIRES	5.0	2.1×10^{-3}	3.1×10^{-3}	1.74×10^{-2}	1.8×10^{-4}	2.7×10^{-4}	7.1
CGS	17.6	2.1×10^{-3}	3.1×10^{-3}	1.74×10^{-2}	6.4×10^{-4}	9.5×10^{-4}	24.9
SIRTf	1.9	2.1×10^{-3}	3.1×10^{-3}	6.53×10^{-3}	2.6×10^{-5}	3.8×10^{-5}	1

$\tau_{\text{straf}} = 6.9 \times 10^{-3}$). The low background flux was estimated by scaling the flux for the high background case by the ratio of the offsets measured for both configurations. The estimated flux on the different detectors is tabulated in Table 2 for each background configuration. The estimated background in the AIRES instrument on a $2\text{mm} \times 2\text{mm}$ detector at $88 \mu\text{m}$ is approximately 10^8 photons/second. It is worth noting that during these tests the flux on the AIRES array in the low background configuration was $\sim 5 \times$ larger than the expected background on SOFIA.

Table 2. Estimated flux per pixel at 88 μm

Array	Low Background Flux (10^6 photon/sec)	High Background Flux (10^6 photon/sec)	Signal Flux (10^6 photon/sec)
AIRES	500	950	1.0
SIRTf	60	130	0.6
CGS	1600	3300	3.5

3.2. Optimum Operating Conditions

We took noise measurements in both the high and low background configurations and signal measurements with the AIRES and SIRTf arrays for a range of temperatures and detector biases (2.2K - 3.9K, 25mV - 100mV) in order to determine the optimum operating points. The signal was chopped at 12Hz. We took noise measurements in 3 frequency bands: 6-10 Hz, 14-18 Hz, and 22-26 Hz. The optimum operating points (maximizing signal to noise) are shown in Table 3. There was little variation in optimum operating point with noise frequency band. There is some variation in operating point with background level. We used these operating points for all subsequent measurements.

Previously determined optimum operating points were used for the CGS detectors. Given the interelectrode distances for these detectors, these optimum operating points are consistent with those found by Ref.7 and 8 for identical detector materials.

Table 3. Optimum Operating Temperature and Bias at 88 μm

Array	Low Background	High Background
AIRES	3.3K, 50 - 100mV	3.6K, 50 - 100mV
SIRTF	3.0 - 3.3K, 75 - 100mV	3.0 - 3.3K, 50 - 75mV

3.3. Detector Performance

3.3.1. Wavelength response

Seven measurements, closely spaced in wavelength, were taken at 6 widely spaced wavelengths. The measurements within each set of seven measurements were averaged together. The resulting values are plotted in Fig. 3. The error bars represent the standard deviation of the distribution of measurements in each wavelength band. In the third panel in Fig. 3 we have divided out the blackbody spectrum in order to obtain a better picture of the detector's wavelength response. Since the wavelength response of the spectrometer has not been removed, the absolute response with wavelength is not adequately determined by these results. However, the relative response between the detector types should be quite accurate.

The wavelength response of the AIRES and CGS detectors are quite similar - as expected since they have similar material (Ge:Sb). The SIRTF (Ge:Ga) detectors have better response at shorter wavelengths and worse response at longer wavelengths than the Ge:Sb detectors. This difference in wavelength response with material was also seen by Ref. 7 and 8.

3.3.2. Channel spectra

The CGS instrument is largely free of channel spectra for many wavelength/filter combinations (see the CGS and AIRES response in Fig. 4). This implies that the AIRES and CGS detectors are free of fringing and that the filters contribute minor fringing at some wavelengths.

The SIRTF detectors exhibited channel spectra in all of the scans we took (see Fig. 4). Variations in wavelength (50 - 102 μm), filters, source size (0.325mm - 1.25mm), and source location (centered, or decentered by 0.5 mm along either axis) do not change the measured channel spectra.

Given the wavelengths of adjacent minima, λ_1, λ_2 , the product nd can be calculated (assuming the light is at normal incidence) from

$$nd = \frac{\lambda_2/2}{1 - \lambda_2/\lambda_1}, \quad (1)$$

where n is the index of refraction and d is the thickness of the material producing the fringing. It is also useful to specify the magnitude of the fringing. The fringe visibility, V is defined as

$$V = \frac{I_{max} - I_{min}}{I_{max} + I_{min}} \quad (2)$$

where I_{max}, I_{min} are the maximum and minimum intensity respectively.

For wavelength/filter combinations which do not exhibit fringing in the CGS or AIRES detectors, the SIRTF detectors always exhibit at least one fringing pattern with $\langle nd \rangle = 7.5\text{mm}$. If $n=4$ (value for germanium) then $d = 1.9\text{mm}$. Since both the lenselet and the detectors are $\sim 2\text{mm}$ deep, we conclude that the fringing is probably occurring within the detectors and/or the lenselet. At 63 μm and 102 μm , the data suggest that there are actually two patterns which are close to 180° out of phase with essentially the same period. Table 4 shows the fringe visibility, period, and nd of the channel spectra found in the SIRTF array for several wavelengths.

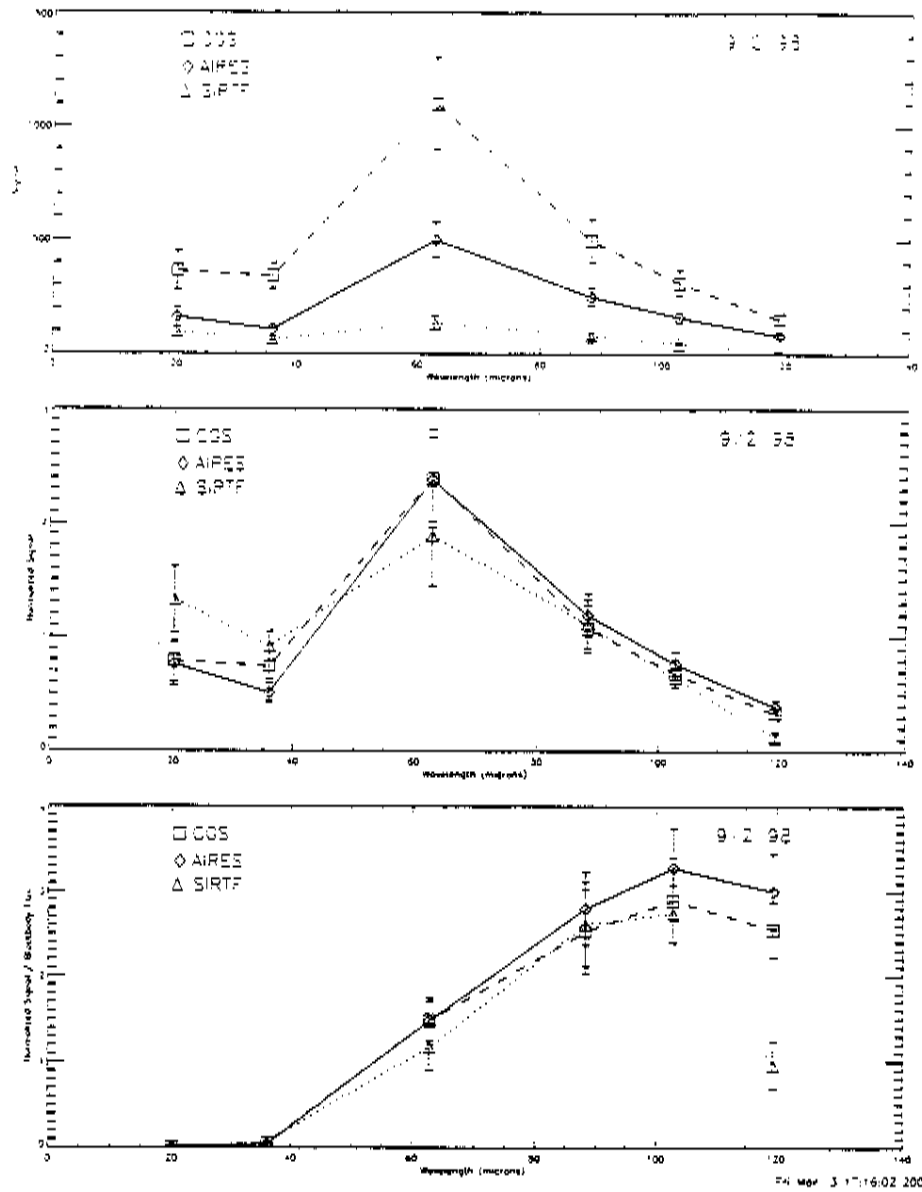


Figure 3. Broad wavelength response of the 3 detector arrays. In the second panel, each measurement was divided by the sum of all the measurements for that detector set in order to bring all data sets onto a similar scale. In the third panel we divided out the source's blackbody spectrum.

3.3.3. Noise

We investigated the noise regime by measuring both the DC offset and the noise of the AIRES and SIRTf detectors while varying the incident radiation (by varying the aperture diameter). Both measurements were taken at the test point of the unit cell. The results are shown in Fig. 5. For both arrays the noise increases with offset as $N \propto O^x$ where $x = 0.45 \pm 0.05$. For background limited performance (BLIP), the expected dependence is $x = 0.5$. This variation from BLIP-like performance might be due to a noise floor (particularly in the data at the smallest offset).

Table 4. SIRTf Channel Spectra

λ (μm)	Fringe Visibility	Period (μm)	nd (mm)
50.00	0.45	0.17	7.3
62.75	0.30	0.26	7.5
101.5	0.35	0.69	7.4

3.3.4. NEP

The noise equivalent power (NEP) is the signal power that gives an rms signal to noise of one in a system that has an electronic bandpass of 1 Hz:

$$NEP = \frac{P}{S/N(df)^{1/2}}, \quad (3)$$

where P is the incident power, S/N is the measured signal to noise and df is the electronic bandpass of the measurement.

Since all arrays used similar preamps and identical A/D's, the measurement bandpasses are equal. The incident power was calculated in Sect. 3.1. We are only going to compare relative values of the NEP, so we will make the simplifying assumption that $df = 1$ Hz. If we define $P_{sirtf} = 1$, then $P_{aires} = 1.8$ and $P_{cgs} = 6.2$ (see Sect. 3.1 and Table 2). Combining the above, the following expressions are obtained for the relative NEP

$$NEP_{SIRTf} = \frac{1}{S/N} \quad (4)$$

$$NEP_{AIRES} = \frac{1.8}{S/N} \quad (5)$$

$$NEP_{CGS} = \frac{6.2}{S/N} \quad (6)$$

Therefore the relative NEPs can be compared by examining $\frac{1}{S/N}$ from the SIRTf array, $\frac{1.8}{S/N}$ from the AIRES array and $\frac{6.2}{S/N}$ from the CGS array. Table 5 lists the mean values of these quantities for the optimum operating conditions. In both background regimes and all noise frequency bands, the NEP is better (i.e. lower) for the SIRTf array.

Even though the detectors may not quite be operating in the background limited regime (Sect. 3.3.3), it is still instructive to examine how the known differences between the detectors can be expected to affect the NEP. In BLIP the expected NEP is

$$NEP_{BLIP} = \frac{2hc}{\lambda} \sqrt{\frac{\phi}{\eta}} \quad (7)$$

where ϕ is the total incident flux in photons per second.⁹ Since we are considering relative NEP, we will consider the ratio of NEP_{BLIP}

$$\frac{NEP_{B,A}}{NEP_{B,S}} = \left(\frac{\phi_A}{\phi_S}\right)^{1/2} \left(\frac{\eta_S}{\eta_A}\right)^{1/2} \quad (8)$$

If we assume $\eta_S = \eta_A$, the photon fluxes estimated in Table 2 can be used to estimate a ratio of NEPs expected in BLIP. We are essentially examining what ratio is expected if the only difference between the arrays is the collecting area. Since the flux decreases with detector area, the NEP of a smaller detector should be better. These estimates are compared to the mean measured values in Table 6.

Since a lower NEP implies a more sensitive detector, when the measured ratio of two NEPs is larger than the predicted ratio, that implies that the detector whose NEP is in the denominator is performing better than predicted relative to the detector whose NEP is in the numerator. From Table 6 we see that the AIRES detectors are performing better than predicted compared to both the SIRTf and CGS detectors. This prediction only takes into account expected differences due to different collecting areas. The variation between the measured values and these calculated values could be due to differences in quantum efficiencies (η).

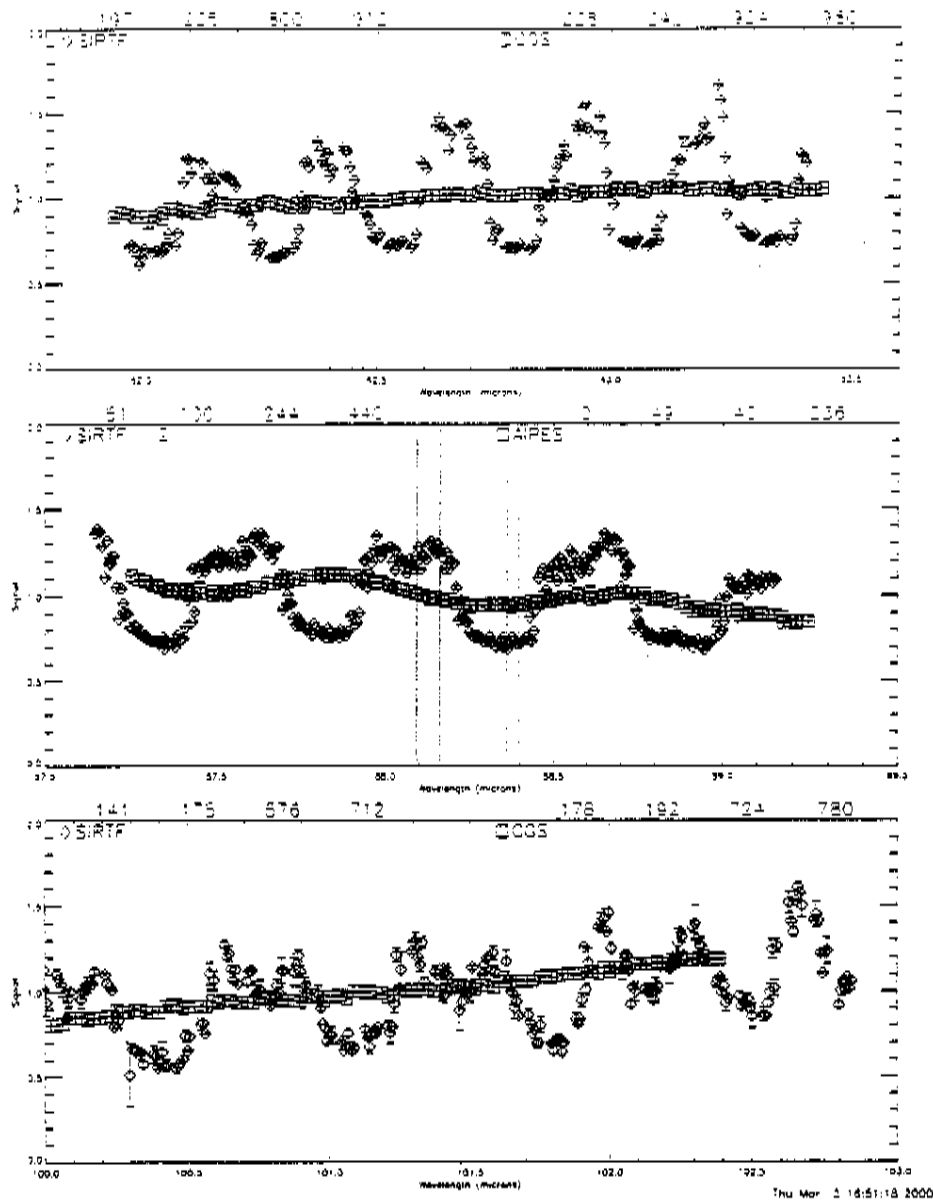


Figure 4. Channel spectra in the SIRT detectors. The set of measurements shown in each frame were taken in identical instrumental configurations. Notice that the CGS and AIRES detectors exhibit little or no channel spectra - implying that the channel spectra measured in the SIRT array are due largely to the detector array itself. The solid vertical lines show the wavelengths which were incident on the SIRT array for most of the characterization data. Similarly the dotted vertical lines show the wavelengths which were incident on the AIRES array during characterization.

4. DISCUSSION

In choosing a detector set for a particular instrument, it is important to consider how well the detector's parameters and performance match the function and constraints of the instrument. Given the plethora of detector parameters (responsivity, quantum efficiency, NEP, DQE) how does one go about making such a decision? Essentially, given a plate scale and background, one wants to minimize the integration time necessary to make a typical measurement.

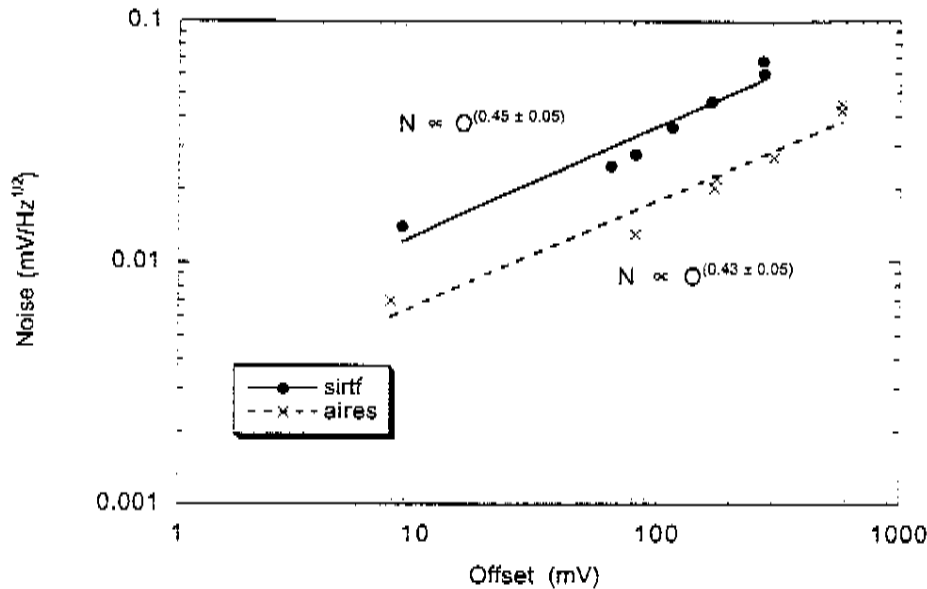


Figure 5. Noise as a function of DC offset for a variety of backgrounds. The errors on the exponents are errors from the fit. The observed relationship between noise and offset is nearly what would be expected for BLIP (an exponent of 0.5). The shallower dependence may be due to a noise floor.

The integration time is related to the NEP, signal power, and desired signal to noise by

$$t = \frac{1}{2}(NEP)^2 \left(\frac{S/N}{P}\right)^2 \tag{9}$$

At first glance, the detectors with the lowest NEP look attractive - but since not all detectors have the same collecting area and plate scales are sometimes fixed by other considerations, before a detector set can be chosen, we must account for the varying powers which will fall on a detector. For the case of an extended source, the incident power can be written as

$$P = A_{det} E. \tag{10}$$

where A_{det} is the collecting area of the detector and E is the incident power in W/area. E is set by the desired source flux and the plate scale of the instrument. Equation (9) can now be rewritten as

$$t = \frac{1}{2} \left(\frac{NEP}{A_{det}}\right)^2 \left(\frac{S/N}{E}\right)^2 \tag{11}$$

If the plate scale cannot be adjusted to match the detectors, the ratio of required integration times is given by

$$\frac{t_1}{t_2} = \left(\frac{NEP_1}{NEP_2}\right)^2 \left(\frac{A_2}{A_1}\right)^2 \tag{12}$$

In AIRES, the optical system is designed for a 2mm pixel pitch. Altering the $f/\#$ to provide a plate scale matched to the smaller SIRTf pitch would be extremely difficult due to space limitations. Comparing the integration times required by the AIRES and SIRTf array yields

$$\frac{t_A}{t_S} = \left(\frac{1}{0.5}\right)^2 \left(\frac{0.75^2}{2^2}\right)^2 = 0.1. \tag{13}$$

Even though the SIRTf detectors exhibit a better NEP than the AIRES detectors, in our application, where it would be difficult to match the plate scale to SIRTf's smaller pitch, the AIRES array is a better choice.

Table 5. Measured Relative NEP

AIRES			SIRTF			CGS	
T(K)	V _b (mV)	$\frac{NEP}{S/N}$	T(K)	V _b (mV)	$\frac{NEP}{S/N}$	T(K)	$\frac{NEP}{S/N}$
Low Background, 6-10Hz							
3.28	50	0.050	2.96	75	0.026	3.3	0.109
3.30	75	0.048					
3.30	100	0.051					
Low Background, 14-18Hz							
3.28	50	0.045	2.96	75	0.023	3.0	0.093
3.30	75	0.042	2.97	100	0.028		
3.30	100	0.043	3.27	75	0.021		
			3.27	100	0.022		
Low Background, 22-26Hz							
3.28	50	0.039	3.27	100	0.017	3.0	0.077
3.30	75	0.036					
3.30	100	0.036					
High Background, 6-10Hz							
3.60	50	0.074	2.26	50	0.053	3.3	0.200
3.61	75	0.074					
3.61	100	0.074					
High Background, 14-18Hz							
3.60	50	0.068	3.27	50	0.048	3.3	0.172
3.61	75	0.066	3.27	75	0.045		
3.61	100	0.068					
High Background, 22-26Hz							
3.60	50	0.060	2.96	75	0.040	3.3	0.147
3.61	75	0.060	3.27	75	0.037		
3.61	100	0.060					

Table 6. Predicted and Mean Relative NEP

Ratio	Low Background				High Background			
	$\frac{\sigma_1}{\sigma_2}$	$\frac{NEP_1}{NEP_2}$	BLIP	$\frac{NEP_1}{NEP_2}$ measured	$\frac{\sigma_1}{\sigma_2}$	$\frac{NEP_1}{NEP_2}$	BLIP	$\frac{NEP_1}{NEP_2}$ measured
SIRTF / AIRES	0.1	0.4		0.5	0.2	0.4		0.7
CGS / AIRES	3.2	1.8		2.2	3.5	1.9		2.6

Another consideration for choosing detectors for AIRES is that they must be well suited for high resolution spectroscopy. The channel spectra in the SIRTF detectors make them a poor match for spectroscopy.

Although the SIRTF array would be an excellent choice for a lower spectral resolution application with a properly matched plate scale, a cavity/cone design similar to our prototype is better suited for use in AIRES.

5. PROTOFLIGHT ARRAY DESIGN

Given the above results, we have designed a 16x24 array based on the 3x3 prototype discussed above. The design is shown in Figure 6. The cavity and cone geometry has been preserved from the 3x3 prototype. The minor differences between the 3x3 and 16x24 array designs were made to either expand the design to a larger format or to improve the ease and reliability of manufacture. The array is built up in modules of 2x24 detectors. The detectors are glued onto an alumina board, which is in turn glued onto the cavity block. Two cavity blocks attach to each cone block and readout frame forming a module. A cryogenic multiplexer with a capacitive transimpedance amplifier (CTIA) unit cell, the SBRC 190, has been developed to read out these arrays. Two multiplexers will sit on a substrate which

is mounted to each readout block. Wire bonds will carry the detector signals from the detector mounting board to the readout substrate. The signals from the readouts are made available through a Nanonics connector on the back of the readout frame. We expect the 16×24 will perform similarly to the 3×3 prototype.

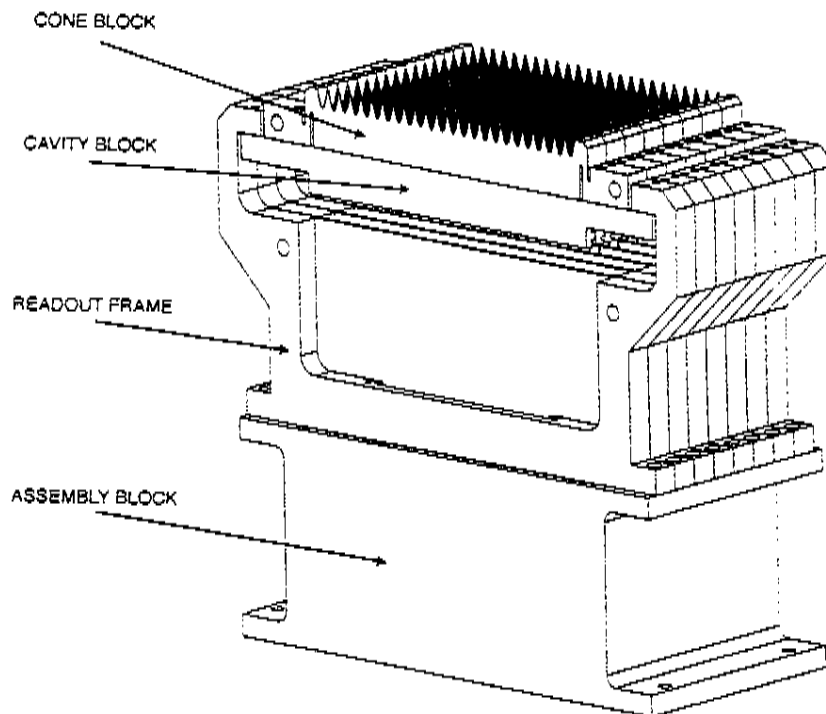


Figure 6. Protoflight 16×24 AIREs array. The cone blocks and the readout frames both fasten onto the same surface on the Molybdenum cavity blocks to facilitate accurate assembly. The detectors are glued onto an alumina board (not visible in this view) which is then glued onto the cavity block. The cone blocks are fastened back end of the readout blocks all fasten to a Cu assembly block.

ACKNOWLEDGMENTS

We thank Erick Young of University of Arizona for providing the 1×32 array of SIRTf detectors for these tests. AIREs is funded by a grant from the Universities Space Research Association for development of SOFIA instruments. J.D. acknowledges support from NASA/Ames Research Center research interchange grant NCC2-647.

REFERENCES

1. E. T. Young, M. Scutero, G. Rieke, T. Milner, F. J. Low, P. Hubbard, J. Davis, E. E. Haller, and J. Beeman, "Far-infrared focal plane development for sirtf," *Proc. of SPIE* 1684, pp. 63-74, July 1992.
2. E. T. Young, M. J. Scutero, G. H. Rieke, and J. T. Davis, "Construction of the large-format far-infrared array for sirtf," *Proc. of SPIE* 2475, pp. 441-448, June 1995.
3. E. T. Young, J. T. Davis, C. L. Thompson, G. H. Rieke, G. Rivlis, R. Schnurr, J. Cadien, L. Davidson, G. S. Winters, and K. A. Kormos, "Far-infrared imaging array for sirtf," *Proc. of SPIE* 3354, pp. 57-65, Aug. 1998.
4. E. F. Erickson, S. Matthews, G. C. Augason, J. R. Houck, M. O. Harwitt, D. M. Rank, and M. R. Haas, "All aluminum optical system for a large cryogenically cooled far infrared echelle spectrometer," in *Cryogenic Optical Systems and Instruments*, *SPIE* 509, pp. 129-139, 1984.

5. E. F. Erickson, J. R. Houck, M. O. Harwitt, D. M. Rank, M. R. Haas, D. J. Hollenbach, J. P. Simpson, and G. C. Augason, "A fir cooled grating spectrometer for the kuiper airborne observatory," *Infrared Physics* **25**, pp. 513-516, 1985.
6. E. F. Erickson, M. R. Haas, J. A. Baltz, S. W. J. Colgan, D. H. Lynch, M. E. McKelvy, and J. Wolf, "Far infrared detector arrays for a sofia echelle spectrometer," in *Submillimeter and Far-Infrared Space Instrumentation, Proc. 30th ESLAB Symp.*, pp. 41-44, 1996.
7. J. W. Beeman, W. L. Hansen, O. D. Dubon, and E. E. Haller, "High performance antimony-doped germanium photoconductors," *Infrared Physics & Technology* **37**, pp. 715-721, 1996.
8. J. W. Beeman, W. L. Hansen, and E. E. Haller, "Extrinsic germanium photoconductors for far-ir astronomy: Research results and works in progress," in *Submillimeter and Far-Infrared Space Instrumentation, Proc. 30th ESLAB Symp.*, pp. 21-24, 1996.
9. G. Rieke, *The Detection of Light from the Ultraviolet to the Submillimeter*. Cambridge University Press, Cambridge, 1994.